

0017-9310(94)E0071-2

Mass transfer in induction plasma reactors

MOHAMED RAHMANE, GERVAIS SOUCY and MAHER I. BOULOS†

Plasma Technology Research Center (CRTP), Department of Chemical Engineering,
Université de Sherbrooke, Sherbrooke, Québec, Canada J1K 2R1

(Received 26 October 1993 and in final form 3 February 1994)

Abstract—A theoretical and experimental study of mass transfer and mixing between a cold jet and a plasma stream is presented for an induction plasma reactor. The concentration profiles of a tracer gas (cold jet), injected axially in the main flow of the plasma, are measured along the centerline of the reactor. Through the application of a turbulent numerical model, concentration, temperature and flow fields are computed. By comparing the measured concentration profiles and the results of the modelling study, it is possible to deduce an effective mass diffusivity for the tracer gas in the mixture and thus calibrate the mathematical model. This work represents a first step in the study of diffusion and mass transfer phenomena under plasma conditions.

1. INTRODUCTION

NUMEROUS studies have been reported in the literature dealing with momentum and heat transfer phenomena in plasma reactors, whether dc plasma jet, induction plasma or transferred arc type. These have mostly dealt with the modelling and measurement of the flow and temperature fields resulting from the interaction of the plasma flow and (a) the walls of the confining chamber, (b) the substrate, in the case of plasma spraying studies, (c) the interaction of multiple plasma jets or (d) plasma flows and cold jets.

Attention has also been given to the interaction between a plasma flow and the particles dispersed in the flow, under both dilute and dense loading conditions. Comprehensive reviews on the subject have been presented by Pfender [1], Fauchais *et al.* [2] and Boulos [3].

Far less attention has been generally given to the important phenomena of mass transfer, which, with the exception of the recent studies by Soucy [4, 5] and Njah *et al.* [6, 7], has been generally overlooked. Earlier experimental studies of mixing and mass transfer under plasma conditions, were made in 1970 by Dundas [8] and 1975 by Barnes [9].

In this paper, a study of mass transfer phenomena in an induction plasma system is presented, and includes the results of experimental measurements of concentration fields, resulting from the interaction of a cold jet and a plasma stream. By comparing the measurement results with the predictions of a 2-D turbulent-LTE model, it became possible to deduce an effective mass diffusion coefficient for these conditions.

A preliminary study of mixing and mass transfer under ambient temperature was used as a calibration

method for the determination of diffusion coefficient under plasma conditions. This is possible because the measurement procedure for the tracer gas concentration distribution is similar in both cases.

2. EXPERIMENTAL SETUP

The experimental apparatus used for the measurement of binary diffusion coefficient of argon into air at room temperature is illustrated in Fig. 1. Air (the main gas flow) was pumped at the rate of 1189 slpm into a circular cross section tube, 80 mm I.D., 1000 mm long (Fig. 1(a)). This arrangement provided an air stream at a mean flow velocity of about 4 m s^{-1} and Reynolds number of 20 000. In the region where the flow was well developed, argon (tracer gas) was injected axially through a 2 mm I.D. tube along the centerline, at a small flow rate (1.45 slpm) so that the main air flow velocity profile would not be modified. The gas sampling system consisted of a stainless steel probe (1.6 mm I.D.) which could be moved step wise in both axial and radial directions and the sampled gas was transported to the composition analysis system (Fig. 1(b)), a VG Micromass PC 300 D quadrupole mass spectrometer (MS), with mass range of 1 to 300 amu. The vacuum in the MS is maintained at an absolute pressure of 10^{-3} – 10^{-4} Pa by a 50 lps turbomolecular pump backed by a 2-stage rotary mechanical pump. The system is controlled by a IBM PC with the appropriate software.

For measurement of mass transfer under plasma conditions, the experimental setup (Fig. 2) consisted essentially of an induction plasma torch, a reactor system, a gas sampling probe and the mass spectrometer (MS), used for the “on-line” analysis of the sampled gas composition.

The plasma torch, a water-cooled, quartz tube (50 mm I.D., 55 mm O.D.) model, with a 5-turn induction

† To whom correspondence should be addressed.

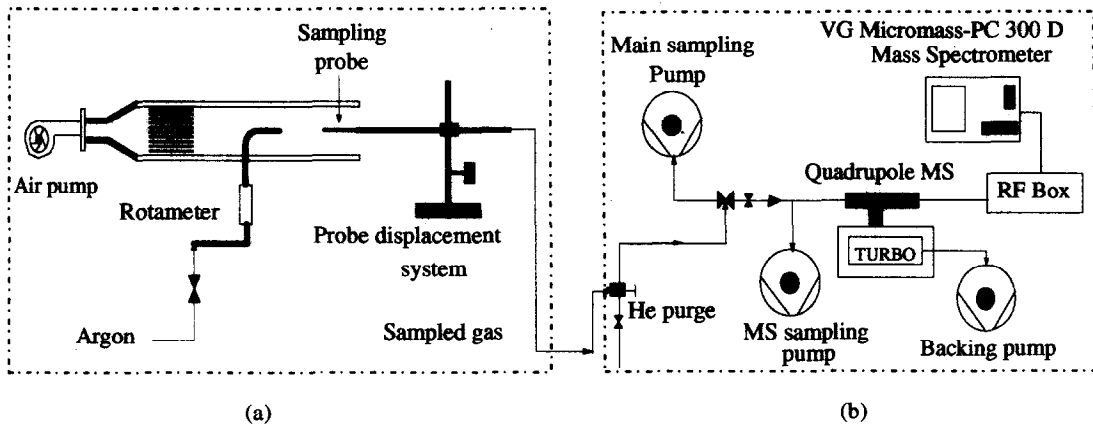


FIG. 1. Experimental set-up for the determination of an effective mass diffusivity of argon into air at ambient temperature. (a) Sampling system; (b) gas composition analysis system (MS).

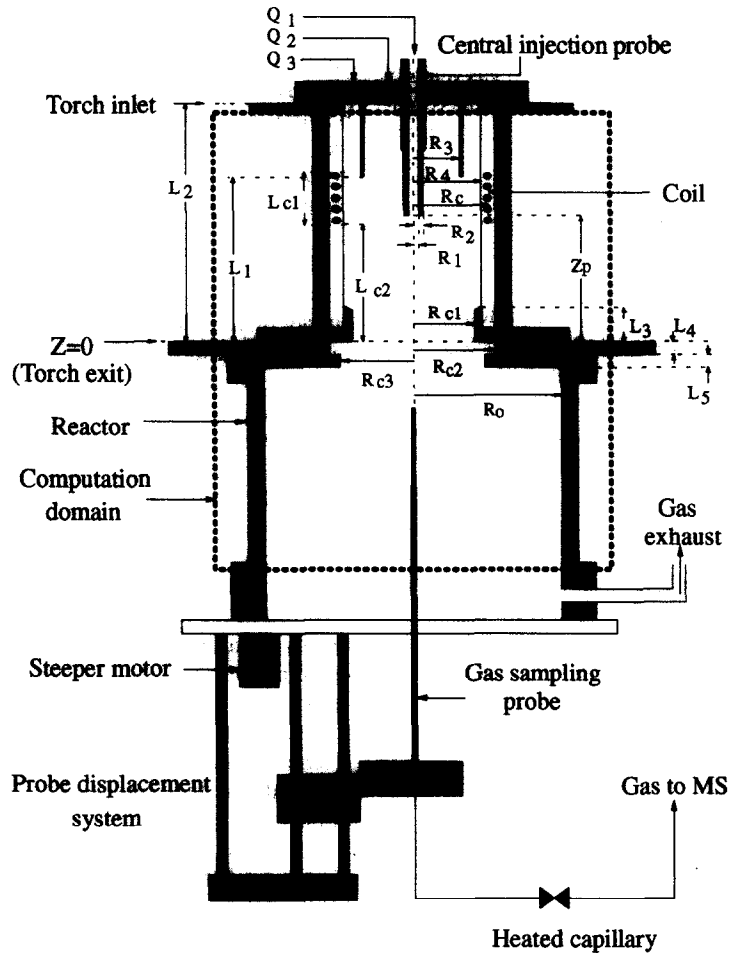


FIG. 2. Schematic diagram of the induction plasma torch-reactor system.

3. MASS TRANSFER ANALYSIS UNDER COLD FLOW CONDITIONS

Mixing and mass transfer phenomena between gas jets under room temperature conditions have been the subject of many researches. A popular technique used

for experimental determination of binary diffusion coefficient between two fluids, was that of injecting a tracer gas (i) axially into the main flow of a second gas (j) in an axisymmetric apparatus as shown in Fig. 1(a). By measuring the spread of the tracer gas concentration, the diffusion coefficient can be

Table 1. Torch and reactor dimensions and operating conditions

| | | |
|--------------------|------------------|-----------------------------------|
| $R_1 = 1.6$ mm | $L_{C1} = 64$ mm | $P = 13, 24$ kW |
| $R_2 = 3.6$ mm | $L_{C2} = 76$ mm | $w = 45$ m s ⁻¹ |
| $R_3 = 20$ mm | $L_1 = 135$ mm | $f = 3$ MHz |
| $R_4 = 25$ mm | $L_2 = 220$ mm | Coil : 5 turns |
| $R_0 = 63.5$ mm | $L_3 = 28$ mm | Q_1 (N ₂) : 15 slpm |
| $R_C = 34$ mm | $L_4 = 19$ mm | Q_2 (Ar) : 59 slpm |
| $R_{C1} = 20.5$ mm | $L_5 = 12$ mm | Q_3 : (Ar) 89 slpm |
| $R_{C2} = 38$ mm | $Zp = 78$ mm | + (H ₂) 9.6 slpm |
| $R_{C3} = 31$ mm | | |

deduced. This technique was used as the calibration method in the present study, but applied to mass transfer under high temperature conditions.

At room temperature, gas density ρ and mass diffusivity D_{ij}^e may be reasonably considered as constant. At an axial position far enough from the tube entrance, the flow is well developed so that gas velocity may be represented by a flat profile (u). A mass balance for species i over a cylindrical ring leads to the following partial differential equation:

$$u \frac{\partial C_i}{\partial z} = D_{ij}^e \left(\frac{1}{r} \frac{\partial}{\partial r} \left(r \frac{\partial C_i}{\partial r} \right) + \frac{\partial^2 C_i}{\partial z^2} \right) \quad (1)$$

where C_i is the molar concentration of i (mole cm⁻³).

Radial and axial diffusion of the tracer gas (i) results from both molecular and turbulent transfer mechanisms. Therefore, the coefficient D_{ij}^e , represents an effective mass diffusivity which is the sum of a molecular coefficient (D_{ij}^m) and a turbulent one (D_{ij}^t):

$$D_{ij}^e = D_{ij}^m + D_{ij}^t. \quad (2)$$

Assuming that the tracer gas molar flow rate Q (mole s⁻¹) is small enough so that the main flow velocity is not deviated appreciably from its flat profile u , the analytical solution of equation (1) is available from the literature [10] and it is given by:

$$C_i(r, z) = \frac{Q}{4\pi D_{ij}^e s} \exp\left(-\frac{u}{2D_{ij}^e}(s-z)\right) \quad (3)$$

where

$$s = \sqrt{(r^2 + z^2)}. \quad (4)$$

Equation (3) may be rewritten as follows:

$$\ln(C_i, s) = \ln\left(\frac{Q}{4\pi D_{ij}^e}\right) - \frac{u}{2D_{ij}^e}(s-z). \quad (5)$$

Knowing the concentration profile $C_i(r, z)$, the linear plot of $\ln(C_i, s)$ vs $(s-z)$ may be used to deduce the effective mass diffusivity D_{ij}^e , from either the intercept or its slope.

4. MASS TRANSFER ANALYSIS UNDER PLASMA CONDITIONS

Under very high temperature conditions, thermodynamic and transport properties of gases are not constant. The general diffusion equation then becomes very difficult, if not impossible, to solve analytically. Under these conditions, the concentration field is, of necessity, dependant on the temperature and flow fields, which means that mass, heat and momentum transfer phenomena must all be studied simultaneously. This is often achieved by means of a numerical method to solve the conservation equations, the method employed in the present study.

4.1. Mathematical model

Flows in plasma reactors occurs very often in both flow regimes, laminar and turbulent. In high temperature regions, the viscosity is so high that a laminar model might provide a reasonable prediction of flow, temperature and concentration fields. In the cooler regions, the contribution of turbulence to transport phenomena is very important and cannot be neglected. A model which takes both flow regimes into account is then necessary for the computation of flow, temperature and concentration fields in plasma reactors. The present study uses the $k-\epsilon$ standard model, as described by Launder and Spalding [11], to represent the turbulent viscosity, the differential kinetic energy of turbulence and the dissipation rate of turbulence equations, and the vector potential concept, to represent the two-dimensional electromagnetic field [12]. The theoretical foundations of this model have been presented previously by Mostaghimi *et al.* [12], El Hage *et al.* [13] and more recently by Chen and Boulos [14, 15]. Improvements have been added in the mass transfer part such as the possibility of using a mixture of several gases and an updated molecular diffusion coefficient. The later was calculated from the algorithm proposed by Bzowski *et al.* [16] which uses results from the theory of statistical mechanics and a combination of an extended principle of corresponding states, with some knowledge of intermolecular potentials.

The assumptions involved in the model are: plasma in local thermodynamic equilibrium (LTE) and optically thin, steady flows, gravity and heat dissipation due to viscosity effects are neglected, two-dimensional flow, temperature and concentration fields, two-dimensional electromagnetic fields and negligible displacement current, density fluctuations are not considered, and Boussinesq's concept of eddy viscosity is adopted for turbulent flow representation.

4.1.1. *Governing equations.* A schematic of the torch-reactor geometry is shown in Fig. 2 and the actual dimensions are given in Table 1. The mathematical statement of the problem is readily given by writing the equations of conservation which are:

1. Continuity

$$\frac{1}{r} \frac{\partial}{\partial r} (r\rho v) + \frac{\partial}{\partial z} (\rho u) = 0. \quad (6)$$

2. Momentum :

$$\rho \left(u \frac{\partial u}{\partial z} + v \frac{\partial u}{\partial r} \right) = \frac{1}{r} \frac{\partial}{\partial r} \left(r\mu^e \left(\frac{\partial u}{\partial r} + \frac{\partial v}{\partial z} \right) \right) + \frac{\partial}{\partial z} \left(2\mu^e \frac{\partial u}{\partial z} \right) - \frac{\partial p}{\partial z} + F_z \quad (7)$$

$$\rho \left(u \frac{\partial v}{\partial z} + v \frac{\partial v}{\partial r} \right) = \frac{1}{r} \frac{\partial}{\partial r} \left(2\mu^e r \frac{\partial v}{\partial r} \right) + \frac{\partial}{\partial z} \left(\mu^e \left(\frac{\partial u}{\partial r} + \frac{\partial v}{\partial z} \right) \right) - \frac{2\mu^e v}{r^2} + \frac{\rho w^2}{r} - \frac{\partial p}{\partial r} + F_r \quad (8)$$

$$\rho \left(u \frac{\partial w}{\partial z} + v \frac{\partial w}{\partial r} \right) = \frac{1}{r} \frac{\partial}{\partial r} \left(r^2 \mu^e \frac{\partial}{\partial r} \left(\frac{w}{r} \right) \right) + \mu^e \frac{\partial}{\partial r} \left(\frac{w}{r} \right) + \frac{\partial}{\partial z} \left(\mu^e \frac{\partial w}{\partial z} \right) - \frac{\rho w v}{r}. \quad (9)$$

F_r and F_z are radial and axial components of the Lorentz electromagnetic force, see equations (20), acting on the plasma gas discharge region.

3. Thermal energy

$$\rho \left(u \frac{\partial h}{\partial z} + v \frac{\partial h}{\partial r} \right) = \frac{1}{r} \frac{\partial}{\partial r} \left(r k^e \frac{\partial h}{\partial r} \right) + \frac{\partial}{\partial z} \left(k^e \frac{\partial h}{\partial z} \right) + P_0 - Q_r \quad (10)$$

where P_0 is the volumetric heat generation due to Joule heating, and Q_r is the radiative power per unit volume.

4. Species conservation

$$\rho \left(u \frac{\partial W_i}{\partial z} + v \frac{\partial W_i}{\partial r} \right) = \frac{1}{r} \frac{\partial}{\partial r} \left(r \rho D_i^e \frac{\partial W_i}{\partial r} \right) + \frac{\partial}{\partial z} \left(\rho D_i^e \frac{\partial W_i}{\partial z} \right). \quad (11)$$

5. Kinetic energy and its dissipation rate

$$\rho \left(u \frac{\partial K}{\partial z} + v \frac{\partial K}{\partial r} \right) = \frac{1}{r} \frac{\partial}{\partial r} \left(r \left(\mu^m + \frac{\mu^t}{\sigma_K} \right) \frac{\partial K}{\partial r} \right) + \frac{\partial}{\partial z} \left(\left(\mu^m + \frac{\mu^t}{\sigma_K} \right) \frac{\partial K}{\partial z} \right) + G_K - \rho \varepsilon \quad (12)$$

$$\rho \left(u \frac{\partial \varepsilon}{\partial z} + v \frac{\partial \varepsilon}{\partial r} \right) = \frac{1}{r} \frac{\partial}{\partial r} \left(r \left(\mu^m + \frac{\mu^t}{\sigma_\varepsilon} \right) \frac{\partial \varepsilon}{\partial r} \right) + \frac{\partial}{\partial z} \left(\left(\mu^m + \frac{\mu^t}{\sigma_\varepsilon} \right) \frac{\partial \varepsilon}{\partial z} \right) + \frac{\varepsilon}{K} (C_1 G_K - \rho C_2 \varepsilon). \quad (13)$$

In equations (12) and (13), the generation rate of kinetic energy G_K is :

$$G_K = \mu^t \left(2 \left(\left(\frac{\partial u}{\partial r} \right)^2 + \left(\frac{\partial v}{\partial r} \right)^2 + \left(\frac{v}{r} \right)^2 \right) + \left(\frac{\partial w}{\partial r} - \frac{w}{r} \right)^2 + \left(\frac{\partial w}{\partial z} \right)^2 + \left(\frac{\partial v}{\partial z} + \frac{\partial u}{\partial r} \right)^2 \right). \quad (14)$$

The effective viscosity μ^t , mass diffusivity D_i^e and thermal conductivity k^e are :

$$\mu^e = \mu^m + \mu^t \quad (15a)$$

$$k^e = k^m + k^t \quad (15b)$$

$$D_i^e = D_i^m + D^t \quad (15c)$$

where superscripts m and t denote respectively molecular and turbulent transport properties. Turbulent viscosity μ^t is calculated from :

$$\mu^t = \rho C_\mu \frac{K^2}{\varepsilon}. \quad (16)$$

The standard model constants are those proposed by Launder and Spalding [11] :

$$C_\mu = 0.09, \quad C_1 = 1.44, \quad C_2 = 1.92,$$

$$\sigma_k = 1.0, \quad \sigma_\varepsilon = 1.3.$$

In addition to this set of conservation equations, two more, aiming for the calculation of electromagnetic field using the vector potential concept, are considered :

$$\frac{\partial^2 A_R}{\partial z^2} + \frac{1}{r} \frac{\partial}{\partial r} \left(r \frac{\partial A_R}{\partial r} \right) - \frac{A_R}{r^2} + \mu_0 \sigma_c \omega A_I = 0 \quad (17)$$

$$\frac{\partial^2 A_I}{\partial z^2} + \frac{1}{r} \frac{\partial}{\partial r} \left(r \frac{\partial A_I}{\partial r} \right) - \frac{A_I}{r^2} - \mu_0 \sigma_c \omega A_R = 0. \quad (18)$$

Assuming that the vector potential A has only its circumferential component A_θ , by means of Maxwell equations, the circumferential components of the electric field E_θ and the radial H_r and axial H_z components of the electromagnetic field may be estimated from :

$$E_\theta = -i\omega A_\theta \quad (19a)$$

$$H_z = \frac{1}{\mu_0 r} \frac{\partial (r A_\theta)}{\partial r} \quad (19b)$$

$$H_r = -\frac{1}{\mu_0} \frac{\partial A_\theta}{\partial z}. \quad (19c)$$

Therefore the quantities F_r , F_z and P_0 involved in the equations for momentum (equations (7) and (8)) and thermal energy, equation (10), are :

$$F_r = \frac{1}{2} \mu_0 \sigma_c \Re (E_\theta H_z^*) \quad (20a)$$

$$F_z = -\frac{1}{2} \mu_0 \sigma_c \Re (E_\theta H_r^*) \quad (20b)$$

$$P_0 = \frac{1}{2} \sigma_c (E_\theta E_\theta^*) \quad (20c)$$

where the superscript * and the symbol \Re denote the

Table 2. Boundary conditions for the conservation equations

| Torch inlet | | | | |
|---|---------|---|---------------------------|--|
| $T = 350 \text{ K}$ | $v = 0$ | $\frac{\partial^2 A_R}{\partial z^2} = \frac{\partial^2 A_1}{\partial z^2} = 0$ | $K = 0.005(u^2 + w^2)$ | $\varepsilon = 1000K^2$ |
| $0 < r < R_1:$ | | $u = Q_1/\pi R_1^2$ | $w = 0$ | $W_{N_2} = 1, W_{H_2} = 0$ |
| $R_2 < r < R_3:$ | | $u = Q_2/\pi(R_3^2 - R_2^2)$ | $w = 45 \text{ m s}^{-1}$ | $W_{N_2} = W_{H_2} = 0$ |
| $R_3 < r < R_4:$ | | $u = Q_3/\pi(R_4^2 - R_3^2)$ | $w = 0$ | $W_{N_2} = 0, W_{H_2} = 3.58 \times 10^{-3}$ |
| Centerline | | | | |
| $\frac{\partial u}{\partial r} = \frac{\partial h}{\partial r} = \frac{\partial W_i}{\partial r} = \frac{\partial K}{\partial r} = \frac{\partial \varepsilon}{\partial r} = v = w = A_R = A_1 = 0$ | | | | |
| Walls | | | | |
| $\frac{\partial W_i}{\partial r} = K = \varepsilon = v = u = w = 0$ | | | | |
| $k^c \frac{\partial T}{\partial r} = \frac{\lambda_w}{\delta_w} (T_s - T_w)$ | | | | |
| $T_w = 350 \text{ K}$ | | | | |
| $A_R = \frac{\mu_0 I}{2\pi} \sqrt{\left(\frac{R_c}{R_0}\right)} \sum_{i=1}^{coil} G(f_i) + \frac{\mu_0 \Omega}{2\pi} \sum_{i=1}^{cv} \sigma_i A_{1,i} S_i G(f_i) \sqrt{\left(\frac{r_i}{R_0}\right)}$ | | | | |
| $A_1 = -\frac{\mu_0 \Omega}{2\pi} \sum_{i=1}^{cv} \sigma_{e,i} A_{R,i} S_i G(f_i) \sqrt{\left(\frac{r_i}{R_0}\right)}$ | | | | |
| Reactor exit | | | | |
| $\frac{\partial W_i}{\partial z} = \frac{\partial(\rho u)}{\partial z} = \frac{\partial v}{\partial z} = \frac{\partial h}{\partial z} = \frac{\partial^2 A_R}{\partial z^2} = \frac{\partial^2 A_1}{\partial z^2} = \frac{\partial K}{\partial z} = \frac{\partial \varepsilon}{\partial z} = 0$ | | | | |

* $G(f)$ is a function of complete elliptic integrals [12]. r_i and S_i are the radius and cross section of the i th control volume (cv).

complex conjugate and the real part of the considered vector respectively.

4.1.2. *Boundary conditions and numerical procedure.* The boundary conditions for equations (6)–(13) and for equations (17) and (18) are summarized in Table 2. The wall-function approach, as described by Launder and Spalding [11], was adopted to represent the fluid behavior near the walls where the flow is almost laminar.

The numerical resolution of the whole set of the differential equations is done using the SIMPLER algorithm [17]. Non-uniform staggered grids (86×68) were used with the majority of nodes concentrated in the zone of plasma generation and the near-wall regions where the gradients of dependant variables are the greatest. The criterion for convergence was that the total normalized residue be less than 0.001.

5. THERMOPHYSICAL PROPERTIES

Molecular transport and thermodynamic properties for pure gases were taken from available data sources [18]. Thermal conductivities k_{mix}^m and viscosities μ_{mix}^m of mixtures are given by the Wilke formula [19]:

$$\gamma_{mix}^m = \frac{\sum_{i=1}^n X_i \gamma_i^m}{\sum_{j=1}^n X_j \Phi_{ij}} \tag{21}$$

in which γ represents the viscosity μ or the thermal conductivity k , and Φ_{ij} a coefficient given by the following equation:

$$\Phi_{ij} = \frac{1}{\sqrt{8}} \left(1 + \frac{M_i}{M_j}\right)^{-1/2} \left(1 + \left(\frac{\mu_i^m}{\mu_j^m}\right)^{1/2} \left(\frac{M_j}{M_i}\right)^{1/4}\right)^2 \tag{22}$$

Thermodynamic properties Γ (such as density or specific heat) of a mixture are given by:

$$\Gamma_{mix} = \sum_{i=1}^n W_i \Gamma_i \tag{23}$$

Molecular mass diffusivities D_{ij}^m were calculated from the correlation established by Bzowski *et al.* [16], based on the theory of statistical mechanics and the principle of corresponding states:

$$D_{ij}^m = \frac{3}{8} \left(\left(\frac{m_i + m_j}{2m_i m_j} \right) \frac{k_b T}{\pi} \right)^{1/2} \frac{k_b T}{p} \frac{(1 + \Delta_{ij})}{\sigma_{ij}^2 \Omega_{ij}^{(1,1)*} (T_{ij}^*)} \tag{24}$$

This formula provides values for molecular diffusivity of pairs of molecular and noble gases and their mixtures. It may be used for high temperature mixtures up to the ionization temperature of the gases considered, which makes it very useful under our operating conditions. The higher-order correction term Δ_{ij} is a complicated function of composition and was simplified to:

$$\Delta_{ij} = 1.3(6C_{ij}^* - 5)^2 \frac{a_{ij}X_{ij}}{1 + b_{ij}X_{ij}} \quad (25)$$

where

$$X_{ij} = \frac{X_i}{X_i + X_j} \quad (26)$$

Expressions for the reduced collision integral $\Omega^{(1,1)*}$ as a function of the non-dimensional temperature $T_{ij}^* = k_b T / \epsilon_{ij}$ and those of the coefficients C_{ij}^* , a_{ij} and b_{ij} may be found in ref. [16].

Once molecular diffusivities are calculated for each i, j gas-pair, the transport coefficient D_i^m for a species i in the mixture is determined by the formula [20]:

$$D_i^m = (1 - X_i) \left/ \sum_{j=2}^n \frac{X_j}{D_{ij}^m} \right. \quad (27)$$

Turbulent coefficients for mass and heat transfer were calculated from turbulent viscosity as:

$$D^t = \frac{\mu^t}{\rho Sc^t} \quad (28a)$$

$$k^t = \frac{\mu^t}{\rho Pr^t} \quad (28b)$$

The turbulent Prandtl number Pr^t was assigned the value of 0.9 and values of 0.7 to 1.0 were applied to the turbulent Schmidt number Sc^t in order to study its effect on concentration profiles.

6. RESULTS AND DISCUSSION

Since the measurement procedure for concentration profile determination of the injected tracer gas under plasma conditions is similar to that used at room temperature, determination of mass diffusivity under cold flow may be used as the calibration technique for the gas composition analysis system.

6.1. Effective mass diffusivity under ambient conditions

Figure 3(a) shows the argon (tracer gas) mole fraction profile $X(r)$ at an axial position of 170 mm from the injection point of the argon. This data were then applied to equation (5), leading to the graph in Fig. 3(b). The latter presents a straight line whose slope is $-u/2D_{ij}^e$. The measured, main flow velocity u was 4 m s^{-1} (Reynolds number = 20 000) which gave an effective mass diffusivity for argon in air of 20.00 $cm^2 s^{-1}$.

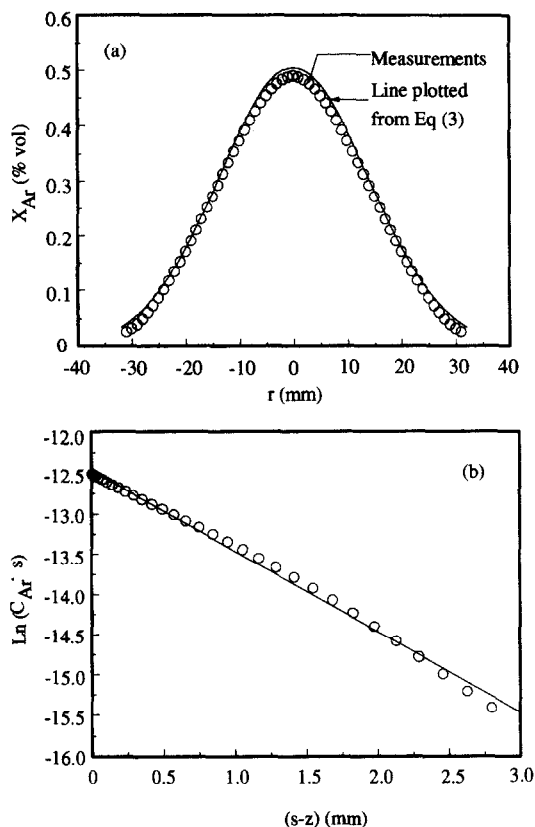


FIG. 3. (a) Radial profile of argon mole fraction in the air flow under room temperature conditions. $z = 170$ mm, $Q_{Ar} = 1.45$ slpm, $Q_{air} = 1189$ slpm, $Re = 20\ 000$. (b) Typical experimental points representing $\ln(C_{Ar})$ against $(s-z)$. The straight line represents equation (5) with $D_{ij}^e = 20\ cm^2\ s^{-1}$.

This value is in good agreement with literature results: the mass diffusivities of CO_2 in air and of H_2 in air measured by Sherwood [10] were found to be 19.00 $cm^2 s^{-1}$.

Figure 3(a) also shows the calculated profile (full line) of the tracer gas concentration (Ar) produced by combining the measured value for mass diffusivity and equation (3). From the comparison of the measured and calculated profiles one may reasonably consider that the value $20\ cm^2\ s^{-1}$, found for the mass diffusivity at room temperature, is acceptable.

6.2. Effective mass diffusivity with plasma conditions

6.2.1. Measured concentration profiles. Nitrogen (tracer gas) concentration profiles were measured in the plasma reactor under the operating conditions summarized in Table 1. Plasma power and reactor pressure effects on the mixing behavior were investigated.

Figure 4 represents the measured N_2 concentration profiles in the absence of plasma, at two different plasma powers (13 kW and 24 kW) and at two different reactor chamber pressures (35 and 93 kPa). In the

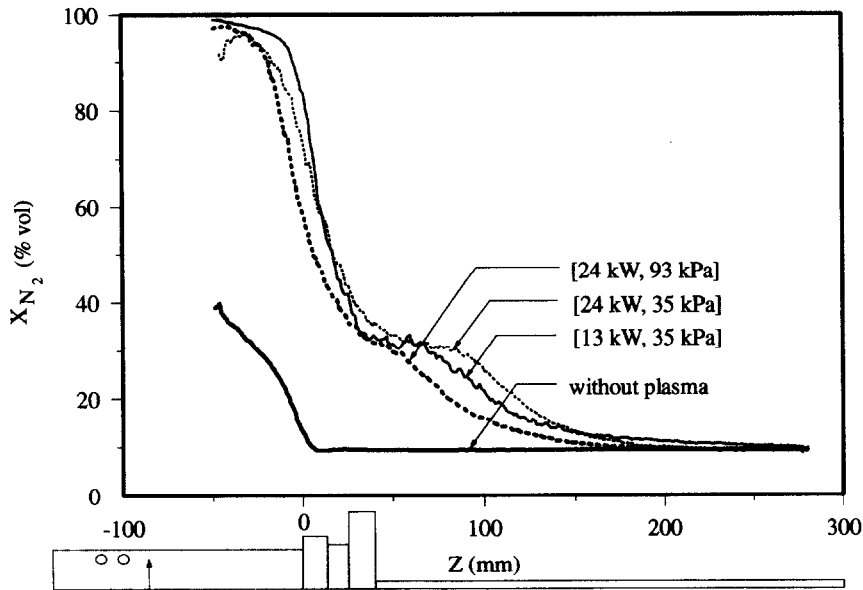


FIG. 4. Effect of the plasma presence, plasma power and reactor chamber pressure on the N_2 concentration profile. The bottom schematic represents the torch-reactor configuration with the probe exit shown by the arrow.

absence of plasma (i.e. cold flow), nitrogen concentration along the axis of the reactor drops rapidly in the first 28 mm from the injection point (pure N_2) located at $Z_p = -78$ mm, to 30 or 40% vol. N_2 at $z = -50$ mm respectively. This rapid drop is mostly due to the strong turbulent flow conditions that prevail up to that point. Beyond $z = -50$ mm, nitrogen concentration along the torch axis continues to drop gradually until it reaches its asymptotic value, corresponding to perfect mixing (8.7% vol. N_2) at the level of the torch exit.

Figure 4 also shows the substantial influence of the plasma presence on the mixing pattern in the torch. The results, plotted for two plasma plate power levels, i.e. 13 kW and 24 kW, reveal that almost no mixing of the auxiliary gas takes place in the first 30 mm from its point of injection. The N_2 concentration in this region remains close to 90–100% vol. N_2 . This is the hottest region of the discharge where the surrounding gas temperature is in the range 9000–10 000 K, as shown by the modeling study (Fig. 5(a)). Over this temperature range, the gas viscosity increases considerably, resulting in the local laminarization of the flow.

Beyond a distance of 30–40 mm from the injection point, the injected auxiliary gas starts to heat while the surrounding plasma cools slightly, resulting in a rapid increase of the mixing and mass transfer phenomena between the two streams, the N_2 concentration along the centerline dropping rapidly in this region. Substantial mixing of the gases does not take place in the low pressure case however until the torch exit level is reached where the auxiliary gas

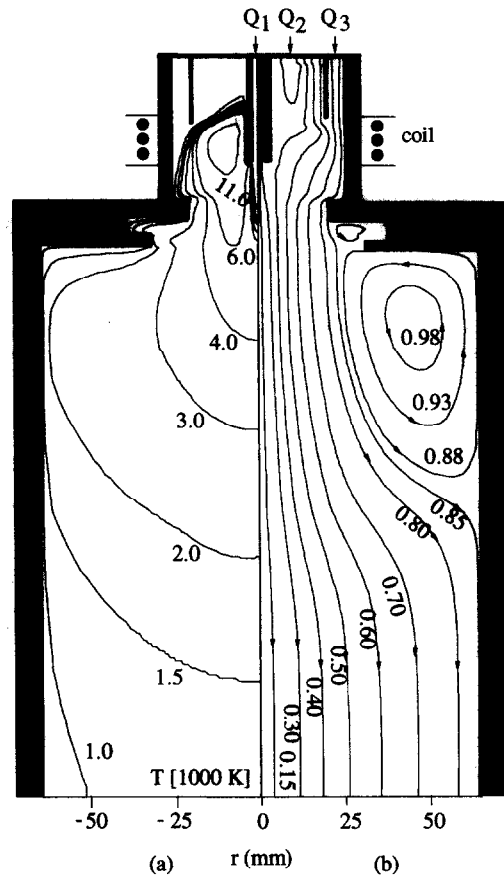


FIG. 5. Computed isotherms (a) and stream lines (b). $P = 24$ kW, $p = 93$ kPa.

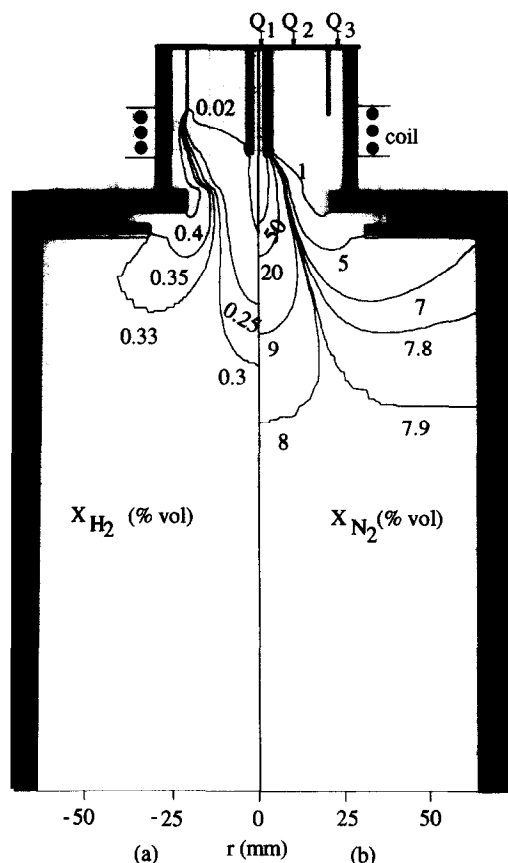


FIG. 6. Computed H_2 (a) and N_2 (b) mole fraction fields. $P = 24 \text{ kW}$, $p = 93 \text{ kPa}$.

concentration on the centerline is still in the range of 80–90% vol.

Within the reactor volume, the input gases cool (temperatures in the range of 3000–4000 K) and mixing is completed within 150 mm from the torch exit. The overall mixing length in this case is therefore between 230 and 250 mm from the gas injection point, which is considerably longer than that observed in the absence of plasma (70–80 mm).

6.2.2. Computed results. Figure 5 shows the computed flow field and isotherms. In Fig. 5(b), three recirculation zones are evident. The first is caused by electromagnetic pumping of the plasma in the coil region. The second and third zones are due to two sudden expansions of the reactor cross section. The third recirculation zone has a large effect on the transport phenomena. Figure 5(a) indicates that the maximum heat loss to the wall occurs in this region (high temperature gradient near the wall). At the reactor exit, the gas temperature is almost uniform (1000 K). Figure 5(a) also suggests that the maximum temperature occurs “off axis” in the discharge zone (11 000 K), but, 100 mm further downstream from the torch exit, the temperature maximum has moved to the centerline.

Figures 6(a) and (b) show respectively the effect on the concentration fields for H_2 , injected with Ar, as

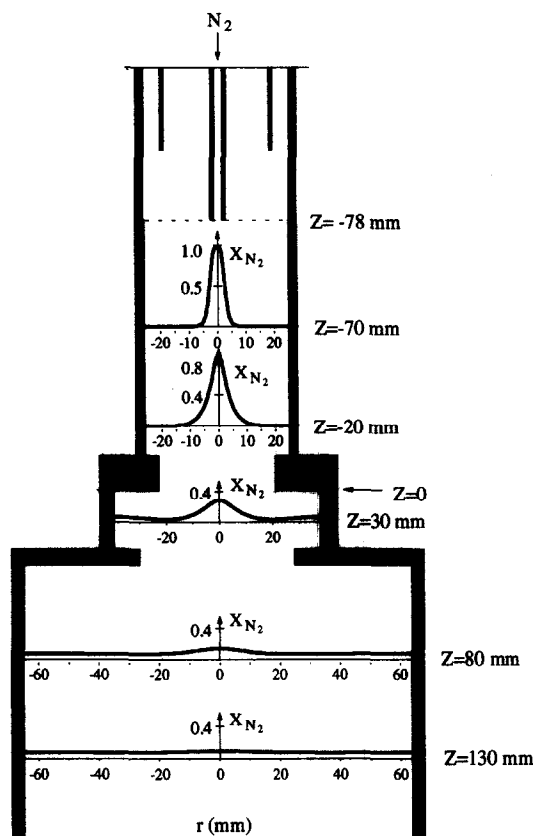


FIG. 7. Illustration of N_2 radial diffusion in the plasma flow showing N_2 mole fraction profiles at different axial positions in the reactor. $P = 24 \text{ kW}$, $p = 93 \text{ kPa}$.

the sheath gas and for the tracer gas (N_2) injected axially via the central tube. One might expect that hydrogen, having the greater molecular diffusion coefficient, would mix faster than nitrogen, but both gases have almost the same mixing length. This is due to the fact that H_2 , initially present in the cooler region of the torch, finds it more difficult to penetrate the “hot” zone because of its high viscosity. These results are consistent with observations made earlier by Dundas [8] on the mixing of the sheath gas with the main flow in an inductively coupled rf plasma.

Figure 7 illustrates the radial diffusion of N_2 at different axial positions in the reactor. It shows that, within the first 50 mm of the tracer gas probe exit, there is almost no radial diffusion of N_2 . Its concentration on the centerline is still as high as 90%. Computed axial velocity at the probe exit is 40 m s^{-1} (Fig. 10(a)), which corresponds to an Re of 8000. Thus the flow regime in this region is turbulent and one would expect stronger mixing in this zone. But, on the other hand, Fig. 5(a) shows that the cold jet is surrounded by the hot plasma (10 000 K) whose viscosity is so high that mass transfer between the N_2 jet and the plasma stream is reduced to that of molecular diffusion. In the next 50 mm the N_2 mole fraction drops rapidly to about 30%, reaching its lower limit (perfect mixing) in the next 50 mm. The

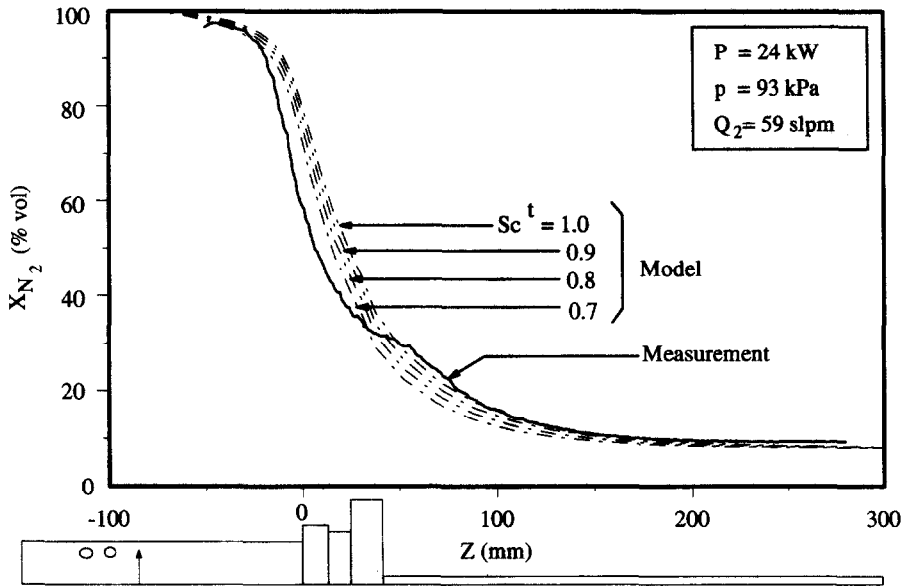


FIG. 8. Effect of turbulent Schmidt number on the computed axial profile of N_2 mole fraction. $P = 24$ kW, $p = 93$ kPa.

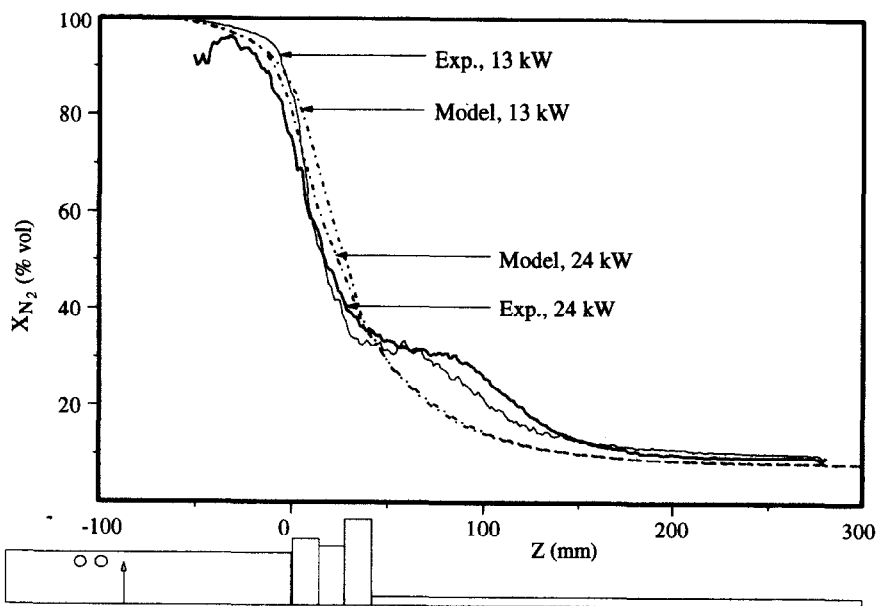


FIG. 9. Comparison of the computed and experimental N_2 mole fraction profiles at two plasma power levels, $P = 13$ kW and 24 kW, $p = 35$ kPa, $Q_2 = 59$ slpm.

gas becomes much cooler (3000–4000 K) and turbulent mass transfer increases.

6.2.3. *Comparison between computed and experimental results.* Figures 8 and 9 show the comparison between the computed and measured N_2 concentration profiles along the axis of the plasma reactor. Two observations from this comparison are of particular interest:

(1) The mathematical model used in this work is considered to be realistic even with all the physical approximations that were applied. This study con-

stitutes the model's first experimental calibration on mass transfer phenomena.

(2) Since the computed and measured N_2 concentration profiles are in good agreement, the effective mass diffusivity for nitrogen in the plasma flow may be calculated by the mathematical model from the turbulent viscosity, using the relation:

$$D_i^e = D_i^m + \frac{\mu_i^t}{\rho Sc^t} \quad (29)$$

where the molecular diffusion coefficient D_i^m is esti-

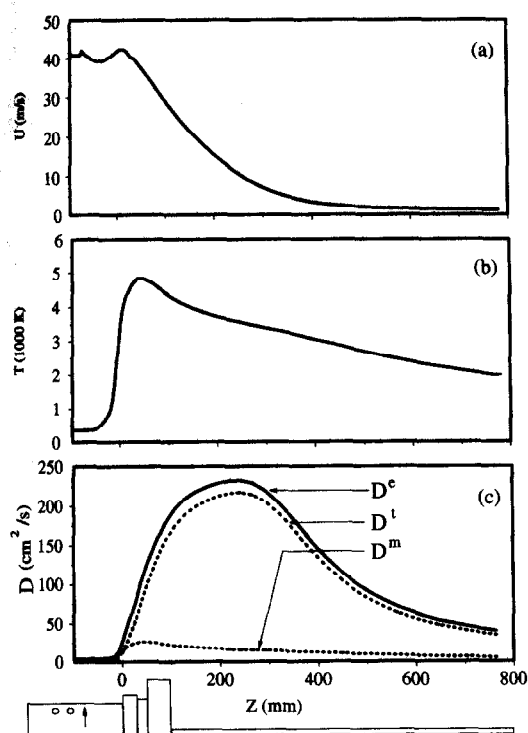


FIG. 10. Profiles of axial velocity (a), temperature (b) and mass diffusivities for N_2 in the mixture (c) for the operating conditions, $P = 24$ kW and $p = 93$ kPa.

mated, as described previously, from equation (24), and the turbulent Schmidt number Sc^t was assigned the value that gives the best representation of the experimental N_2 concentration profile by the model. Figure 8 shows that, with the turbulent Schmidt number equal to unity, the model represents more accurately the experimental profile in the region $z > 50$ mm of the reactor. Smaller values (less than 1.0) give computed profiles which are closer to the measured one in the $z < 50$ mm zone. However, the difference is not significant and an optimal value of 0.8 was attributed to Sc^t for the two other cases (Fig. 9).

Axial velocity and temperature profiles are shown in Figs. 10(a) and (b), respectively. Figure 10(c) represents molecular, turbulent and effective mass diffusivity profiles along the centerline of the torch-reactor system. From the N_2 injection point (shown by the arrow on the bottom schematic) to the torch exit, the centerline temperature is still low and so is the molecular component of mass diffusivity. On the other hand, eddy diffusivity in this zone is also low because of the laminarization of the surrounding plasma. 50 mm downstream of the torch exit, the flow becomes hotter on the centerline, which increases laminar transfer (D^m). But turbulent mass transfer (represented by D^t) became more important because the bulk gases temperature decreased and also because of the sudden expansion at the reactor throat. In the middle zone of the reactor ($z = 250$ mm), D^t rises to its maximum value which is about ten times higher

than D^m . This is in fact the region where the strong recirculating flow occurs, because of the last reactor expansion.

7. SUMMARY AND CONCLUSION

A calibration of the mathematical model used for the prediction of flow, temperature and concentration fields in an rf plasma reactor is accomplished on a mass transfer basis. Comparison between computed and measured N_2 concentration profiles has allowed us to determine an effective mass diffusivity under plasma conditions. Thence, by estimating values for molecular diffusivity from statistical mechanics theory, it has been possible to compare the two mechanisms for mass transfer, i.e. molecular and turbulent, under high temperature plasma conditions. The following specific conclusions can be made:

(1) Mass transfer phenomena between a cold jet of gas injected axially into the discharge zone of an induction plasma torch and the surrounding plasma heated gas is much different from that existing under room temperature conditions. The computed results show that, in the highest temperature zone, mass transfer is mostly achieved by molecular diffusion, while, downstream of the torch exit where the gas has become cooler, turbulence takes over and the mixing between the gas jets is faster.

(2) Turbulent Schmidt numbers close to unity appear to provide a realistic basis for the computation of mass transfer, under plasma conditions.

(3) The mathematical model developed for this study provides a satisfactory representation of the mixing behaviour in comparison to the experimental findings.

Acknowledgements—The authors gratefully acknowledge the financial support of the Conseil de Recherche en Sciences Naturelles et en Génie du Canada (CRSNG) and the Fonds pour la Formation de Chercheurs et l'Aide à la Recherche (FCAR). The authors would like also to thank Dr Peter Lanigan for his contribution to the proofreading of this paper.

REFERENCES

1. E. Pfender, Heat and momentum transfer to particles in thermal plasma flows, *Pure Appl. Chem.* **57**, 1179–1195 (1985).
2. P. Fauchais, A. Vardelle, M. Vardelle, J. F. Coudert and B. Pateyron, Plasma spraying and extractive metallurgy: comparison between mathematical modelling and measurements and between application and development, *Pure Appl. Chem.* **57**, 1171–1177 (1985).
3. M. I. Boulos, The inductively coupled RF (radio frequency) plasma, *Pure Appl. Chem.* **57**, 1321–1352 (1985).
4. G. Soucy, Synthèse de poudres ultrafines de Si_3N_4 par plasma inductif, PhD thesis, Université de Sherbrooke, Sherbrooke, Quebec (1992).
5. G. Soucy, J. W. Jurewicz and M. I. Boulos, Mixing study of the induction plasma reactor—I. Axial injection mode, *Plasma Chem. Plasma Processing* **14**, 43–58 (1944).

6. Z. Njah, J. Mostaghimi, M. Faghir and M. I. Boulos, Study of 3-D mixing of a cold jet with a traverse plasma stream, *Int. J. Heat Mass Transfer*, **36**, 3897–3907 (1993).
7. Z. Njah, J. Mostaghimi and M. I. Boulos, Mathematical modelling of the 3-D mixing in an induction plasma reactor, *Int. J. Heat Mass Transfer* **36**, 3909–3919 (1993).
8. P. H. Dundas, Induction plasma heating: measurements of gas concentrations, temperatures and stagnation heads in a binary plasma system, NASA Contract Report, NASA CR-1527, Washington, DC (1970).
9. R. M. Barnes and S. Nikdel, Mixing of ambient nitrogen in a flowing argon inductively coupled plasma discharge, *Appl. Spectrosc.* **29**, 477–481 (1975).
10. T. K. Sherwood and R. L. Pigford, *Absorption and Extraction* (2nd Edn), p. 42. McGraw-Hill, New York (1952).
11. B. E. Launder and D. B Spalding, The numerical computation of turbulent flow, *Comp. Meth. Appl. Mech. Engng* **3**, 269–289 (1974).
12. J. Mostaghimi and M. I. Boulos, Two-dimensional electromagnetic field effects in induction plasma modelling, *Plasma Chem. Plasma Processing* **9**, 25–43 (1989).
13. M. El-Hage, J. Mostaghimi and M. I. Boulos, A turbulent model for the rf inductively coupled plasma, *J. Appl. Phys.* **65**, 4178–4184 (1989).
14. K. Chen and M. I. Boulos, Turbulence in induction plasma modelling, *J. Phys. D, Appl. Phys.* **27**, 946–952 (1994).
15. K. Chen, Study of induction plasma spraying process, PhD thesis, University of Sherbrooke, Quebec (1993).
16. J. Bzowski, J. Kestin, E. A. Mason and E. J. Uribe, Equilibrium and transport properties of gases mixtures at low density: eleven polyatomic gases and five noble gases, *J. Phys. Chem. Ref. Data* **19**, 1179–1186 (1990).
17. S. V. Patankar, *Numerical Heat Transfer and Fluid Flow*. McGraw-Hill, New York (1980).
18. M. I. Boulos, Thermodynamic and transport properties of argon, nitrogen and oxygen at atmospheric pressure in the temperature range 300–20 000 K, CRTP Internal Report 90-1 (1990).
19. R. B. Bird, W. E. Stewart and E. N. Lightfoot, *Transport Phenomena* (1st Edn), p. 24. John Wiley, New York (1960).
20. R. B. Bird, W. E. Stewart and E. N. Lightfoot, *Transport Phenomena* (1st Edn), p. 571. John Wiley, New York (1960).